

# Flowfield Measurements in a Single Row of Low Aspect Ratio Pin Fins

Jason K. Ostanek<sup>1</sup>  
e-mail: jostanek@psu.edu

Karen A. Thole  
e-mail: kthole@engr.psu.edu

Mechanical and Nuclear Engineering Department,  
Pennsylvania State University,  
University Park, PA 16803

*Pin-fin arrays are commonly used as compact heat exchangers for cooling the trailing edge of gas turbine airfoils. While much research has been devoted to the heat transfer characteristics of various pin-fin configurations, little work has been done to investigate the flowfield in pin-fin arrays. Such information may allow for further optimization of pin-fin configurations. A new pin-fin facility at large scale has been constructed to allow optical access for the use of nonintrusive measurement techniques such as laser Doppler velocimetry and time-resolved, digital particle image velocimetry. Using these techniques, the flow through a single row of pin fins having a height-to-diameter ratio of 2 and span-to-diameter ratio of 2.5 was investigated. Results showed that the length of the wake region decreased with increasing Reynolds number. At higher Reynolds numbers, Kármán vortices developed closer to the pin fins than for single, infinitely long cylinders. Transverse fluctuations correlated well with endwall heat transfer indicating that the Kármán vortices play a key role in energy transport. [DOI: 10.1115/1.4004755]*

## Introduction

Modern gas turbine engines operate with turbine inlet temperatures exceeding the melting temperature of the airfoils. Operation in such high temperature environments is made possible through advanced airfoil materials and active cooling. The current state-of-the-art in modern airfoil cooling includes: shaped film-cooling holes, impingement cooling, and advanced internal cooling passages.

Internal cooling passages, which are cast integrally into the airfoils, use compressor bleed air as the medium to remove heat from the parent material. Flow turbulators such as ribs and pin fins are manufactured into the cooling passages as heat transfer enhancement features. Because the thermal load varies around the airfoil, cooling passages are designed specific to the region of the airfoil. For example, at the trailing edge, the external hot-gas path imposes a large thermal load and the parent material is characteristically thin. In this region, pin-fin arrays provide a robust solution due to high heat transfer rates and structural integrity from bridging the pressure and suction sides of the airfoil.

Over the past several decades, pin-fin research has established a broad understanding of the effects of Reynolds number, array geometry, and rotation on heat transfer. A deeper understanding of the turbulent flow can provide insight into ways of providing the required heat transfer coverage while simultaneously reducing the amount of coolant needed. Due to the complex nature of the flow and turbulence in such geometries, detailed analysis of the flowfield requires the use of computationally intensive numerical models or the use of detailed flowfield measurement techniques.

The present work employs laser Doppler velocimetry (LDV) and time-resolved, digital particle image velocimetry (TRDPIV) to make highly resolved flowfield measurements in a single row of pin fins. The objective of this study is to investigate the flowfield in a single row of pin fins and determine which flow structures contribute most to heat transfer.

## Previous Studies

Pin-fin arrays have been researched for several decades and have contributed significantly to advancing turbine component durability to the level it is today. Flow through pin fins is closely related to more fundamental flows such as single, infinitely long cylinders in crossflow and wing-body junction flows. While highly detailed measurements have been made for such flows, detailed flowfield measurements for pin fins, or cylinders confined in a duct, are limited. The majority of literature pertaining to pin-fin arrays focuses on the heat transfer characteristics for various geometric configurations and flow conditions.

As mentioned, the goal of this work was to determine which flow features contribute to heat transfer in pin-fin arrays. In staggered arrays of long-tube cylinders, the fins experience enhanced heat transfer from the wake turbulence generated by upstream rows [1]. Similarly, in staggered pin-fin arrays, the row-by-row variation in freestream turbulence increases up to row three [2–4] and agrees reasonably well with the row-by-row variation in heat transfer [5,6]. Ames et al. [6] performed spatially resolved heat transfer measurements and reported that the local heat transfer enhancement was due to the local freestream turbulence as well as local secondary flows, such as the horseshoe vortex. In a similar study, Lyall et al. [7] reported spatially resolved heat transfer measurements for single rows of pin fins with  $H/D=1$  and  $S/D=2, 4, \text{ and } 8$ . For  $2 \leq S/D \leq 8$ , both wake turbulence and the horseshoe vortex contribute to heat transfer. Lyall et al. found that  $S/D=2$  produced the greatest heat transfer augmentation due to the local flow acceleration and interaction between the pin-fin wakes. Ozturk et al. [8] made detailed flowfield measurements for a single, low aspect ratio cylinder confined in a duct where  $H/D=0.4$ . The authors reported highly three-dimensional and unsteady flow in the cylinder wake. Ozturk et al. found that the instantaneous state of the horseshoe vortex system is not symmetric with respect to the channel centerline. The number, size, and strength of vortices vary randomly with time. No comparisons with cylinder surface and endwall heat transfer were reported.

Heat transfer characteristics in pin-fin arrays have been quantified for geometric variations such as height-to-diameter ratio and pin-fin shape. Height-to-diameter ratio plays an important role in the ratio of wetted pin-fin and endwall surface area. For  $H/D \leq 2$  there is no significant impact of height-to-diameter ratio on array heat transfer [9,10]. For  $H/D > 2$ , array heat transfer increases

<sup>1</sup>Corresponding author.

Contributed by the International Gas Turbine Institute (IGTI) of ASME for publication in the JOURNAL OF TURBOMACHINERY. Manuscript received July 18, 2011; final manuscript received July 27, 2011; published online May 31, 2012. Editor: David Wisler.

with increasing  $H/D$  and greater increases occur at lower Reynolds numbers [9,10]. The use of streamlined pin fins has been considered as an alternative to circular pin fins. When streamlined pin fins are aligned with the flow, heat transfer and pressure drop are expectedly reduced for oblong [11] and for ellipse [12] shaped pin fins. Detailed flowfield measurements reported by Uzol and Camci [12] showed the classic differences between bluff and streamlined bodies including: delayed boundary layer separation, reduced turbulent kinetic energy production, and a narrower wake region. For the streamlined pin fins, the heat transfer was concentrated directly behind the pin fins; while for circular pin fins the heat transfer was more uniformly distributed in the transverse direction.

Much effort has been devoted to endwall and pin-surface heat transfer in pin-fin arrays. Several studies have investigated the flowfield in the pin-fin arrays, but little work has been done to determine the relationship between flowfield structure and array heat transfer. The present study makes use of detailed flowfield measurement techniques to investigate the turbulent flow through pin-fin arrays in order to determine which flow features contribute most to heat transfer.

### Experimental Setup and Instrumentation

Flowfield measurements were taken in a wide, constant area cross-sectional duct containing a single row of pin fins having  $H/D=2$  and  $S/D=2.5$ . An overall view of the experimental facility is shown in Fig. 1. A variable frequency drive controlled a centrifugal blower capable of 13.2 kPa and  $0.658 \text{ m}^3/\text{s}$ . The blower discharged air to an inlet plenum equipped with a splash plate which prevented jet formation in the test section. Flow entered the test section through a sharp-edge contraction to promote transition to turbulence. For optical access, the measurement region was constructed of glass and polycarbonate. Flow then exited the test section into a downstream plenum equipped with splash plates and a heat exchanger to remove excess heat added to the flow from the blower. Finally, flow passed through a venturi flow meter then returned to the blower inlet.

Operating conditions in the facility were controlled to maintain near atmospheric pressure and temperature in the test section. The gauge pressure in the test section was controlled using relief valves to prevent deformation of the channel walls. The temperature in the test section was controlled by adjusting the flow rate of chilled water through the heat exchanger in the exit plenum.

Experiments were performed at large scale where the channel height and pin-fin diameter were 63.5 and 31.75 mm, respectively. And the channel width-to-hydraulic-diameter ratio was 9.4. Three Reynolds numbers were considered and the spatial resolution of both the LDV and TRDPIV are shown in Fig. 1. Spatial resolutions were quantified by calculating the  $y^+$  values associated with the LDV beam waist and the final TRDPIV grid resolution ( $8 \times 8$  pixels).

**Flowfield Measurements.** Flowfield measurements were made using two-component LDV and TRDPIV techniques. In both cases, di-ethyl-hexyl-sebecat (DEHS) was atomized to  $1 \mu\text{m}$  droplets using a Laskin nozzle aerosol generator described in Raffel et al. [13]. The tracer particles were assumed to experience zero slip velocity as the Stokes number was calculated to be much less than unity for all Reynolds number flow conditions. The particles were injected into the test rig immediately downstream of the blower to promote uniform mixing.

LDV measurements were made with a two-component, fiberoptic system. A 5 W argon-ion laser was passed through a beam separator to produce two beam pairs, where each pair measured one velocity component. One beam per pair was shifted by 40 MHz to allow measurement of reversing flow. The fiber optic probe contained both transmitting and receiving optics and operated in a backscatter arrangement. The probe was fitted with a 2.60 ratio beam expander and a 750 mm lens which produced a measurement volume having major and minor diameters of 850 and  $72 \mu\text{m}$ , respectively. For all LDV measurements, a minimum of 5000 samples were measured over at least 30 s for each component of velocity.

A TRDPIV system was used to capture the instantaneous flow structures. A dual cavity 15 W Nd:YAG laser capable of firing at 10 kHz per laser cavity illuminated the tracer particles while a 2 kHz CMOS camera captured particle images at a spatial resolution of  $1024 \times 1024$  pixels. The time delay between laser pulses was adjusted for each run to obtain a bulk particle displacement of approximately 8 pixels, which was less than one-quarter of the initial interrogation window size. Flow statistics were calculated over at least 1000 image pairs at  $1024 \times 1024$  pixel resolution. The recording rate was varied to optimize sampling frequency and test duration. In each experiment the flow crossed the domain at least 170 times and the Nyquist frequency was at least 8.7 times greater than the measured vortex shedding frequency.

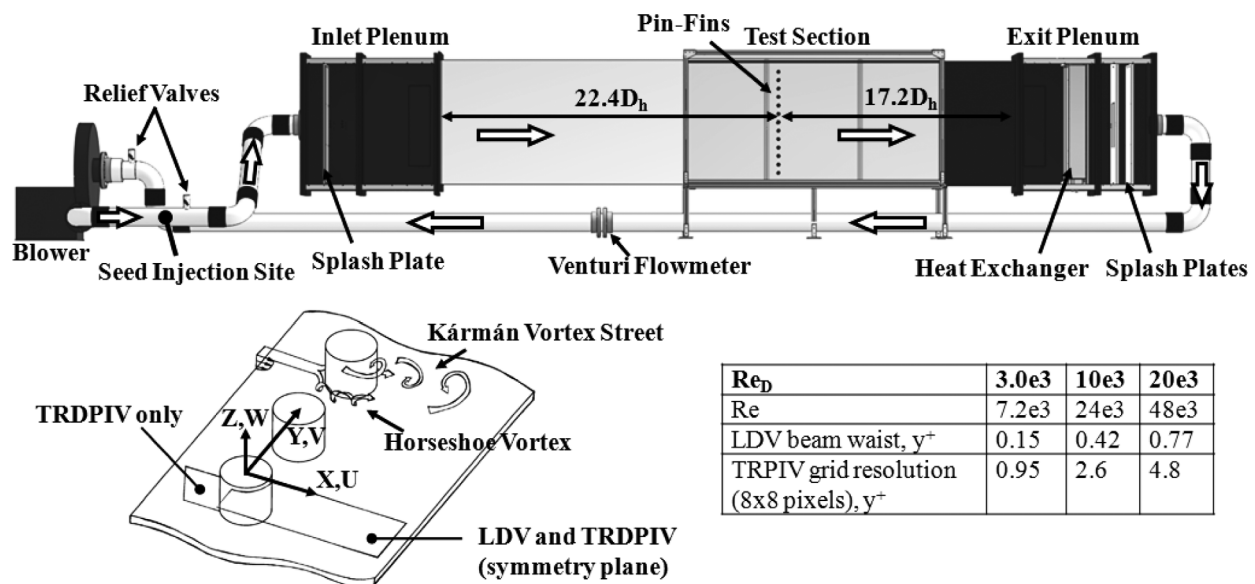


Fig. 1 Schematic of test facility, schematic of measurement planes, and summary of spatial resolution

Images were processed using commercially available software. Signal-to-noise ratio was improved by performing a minimum pixel intensity background subtraction. Images were then processed using a decreasing, multigrid scheme whereby the first interrogation window was set to  $64 \times 64$  pixels with 50% overlap and the final window was set to  $16 \times 16$  pixels with 50% overlap. By default, the processing software halved the window size on intermediate passes. Images were masked to remove test section boundaries, replacing nonvalid regions with zero intensity. Interrogation windows were discarded on the initial pass if a given window was at least 30% masked and were discarded on all subsequent passes if a given window was at least 60% masked. A standard cross correlation was used to determine displacement vectors among image pairs. A fractional window offset with first-order image mapping through bilinear interpolation according to the vector field of the previous pass was performed for intermediate and final passes. The final TRDPIV image processing scheme is shown in Table 1. Vector validation was performed after each pass using a 4-pass median filter similar to Nogueira et al. [14] but with adjustable criteria for removal and re-insertion of possible spurious vectors. For each experiment, the vector validation scheme was checked to ensure that only spurious vectors were removed.

**Uncertainty Analysis.** When estimating uncertainty in Reynolds number, friction factor, and pressure coefficient, bias uncertainty estimates in each measurement were obtained from manufacturer specifications and overall bias uncertainty was estimated using the sequential perturbation method described by Mofat [15]. Bias uncertainties in mean LDV measurements were 1% of the measured mean velocity [16]. Uncertainty in TRDPIV velocity measurements were dominated by in-plane velocity gradients for the image processing techniques used [13]. Velocity bias near vortex cores, where the spatial wavelength may approach the size of the interrogation window, was estimated for  $16 \times 16$  pixel interrogation windows and the spatial wavelength of the horseshoe vortex [17]. Random errors associated with large displacement gradients were also included and were estimated from the maximum instantaneous gradients observed [17]. Precision uncertainties were calculated for a 95% confidence interval for all measurements except for TRDPIV due to the computational resources required for a student's  $t$ -distribution analysis. The precision uncertainty associated with TRDPIV measurements were expected to be low due to the amount of data acquired (at least 170 convective units). The results of the uncertainty analysis are shown in Table 2.

### Validation of Test Facility and Methods

To ensure proper operation of the test facility and accuracy of the measurement techniques, several validation tests were performed. Friction factors for an unobstructed duct were calculated from measured pressure losses. The maximum difference from correlations was measured to be 6.2% for  $15 \times 10^3 < Re < 45 \times 10^3$ .

Velocity profiles through the unobstructed duct were measured using LDV. Figure 2 shows the mean streamwise velocity scaled to inner coordinates. At  $Re = 6.8 \times 10^3$ , there was a slight overshoot in the log-law region due to the transitional nature of the

**Table 1 TRDPIV image processing scheme**

Pass	Window size (pixels)	Overlap	Grid resolution (pixels)	Discrete offset/image deformation
1	$64 \times 64$	50%	$32 \times 32$	No/No
2	$32 \times 32$	50%	$16 \times 16$	Yes/Yes
3	$16 \times 16$	50%	$8 \times 8$	Yes/Yes
4	$16 \times 16$	50%	$8 \times 8$	Yes/Yes

**Table 2 Measurement uncertainties**

Measurement	$Re_D = 3.0 \times 10^3$	$Re_D = 20 \times 10^3$
$Re_D$	$U_{95} = \pm 2.8\%$	$U_{95} = \pm 1.3\%$
$f$	$U_{95} = \pm 15.6\%$	$U_{95} = \pm 2.0\%$
$C_p$ at $\theta = 180$ deg	$U_{95} = \pm 15.1\%$	$U_{95} = \pm 2.9\%$
LDV $- U/U_m$	$U_{95} = \pm 3.0\%$	$U_{95} = \pm 1.1\%$
LDV $- V/U_m$	$U_{95} = \pm 1.3\%$	$U_{95} = \pm 1.1\%$
LDV $- u'/U_m$	$U_{95} = \pm 1.0\%$	$U_{95} = \pm 0.2\%$
LDV $- v'/U_m$	$U_{95} = \pm 0.4\%$	$U_{95} = \pm 0.3\%$
TRDPIV $- U/U_m$	$U_{bias} = \pm 2.3\%$	$U_{bias} = \pm 3.4\%$
TRDPIV $- V/U_m$	$U_{bias} = \pm 2.3\%$	$U_{bias} = \pm 3.4\%$

flow. At  $Re = 45 \times 10^3$ , good agreement to the law-of-the-wall was observed. The friction factor derived from the measured wall shear stress was within 4.6% and 5.1% of unobstructed channel flow at  $Re = 6.8 \times 10^3$  and  $Re = 45 \times 10^3$ , respectively [1]. Figure 3 shows streamwise velocity fluctuations scaled to inner coordinates where good agreement to unobstructed channel flow was observed [18].

After benchmarking the unobstructed duct case, a single row of pins was installed in the test facility. LDV measurements confirmed flow uniformity across the wakes of the pin fins. TRDPIV measurements were compared with those acquired using LDV at several locations. The measurement locations were chosen where

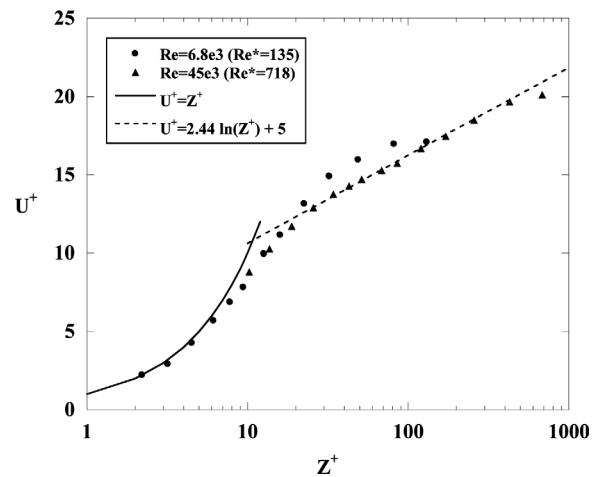


**Fig. 2  $U^+$  versus  $Z^+$  measured using LDV at various Reynolds numbers in unobstructed duct**

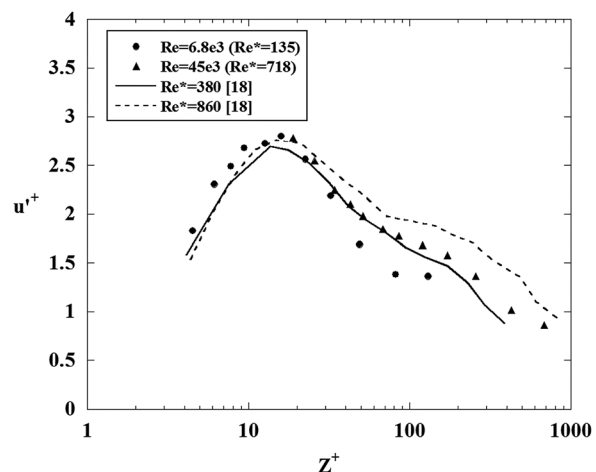


**Fig. 3  $u^+$  versus  $Z^+$  measured using LDV at various Reynolds numbers in unobstructed duct [18]**

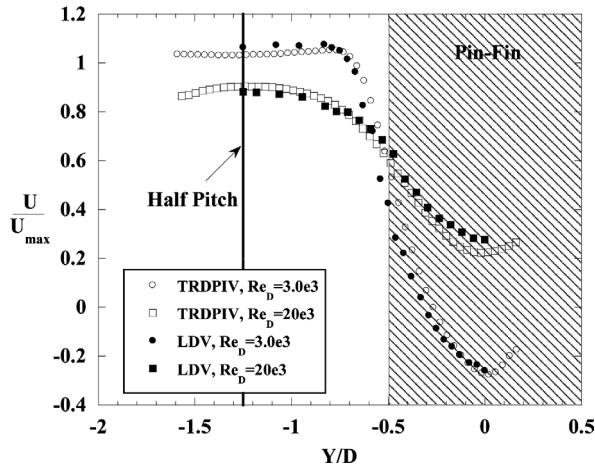


Fig. 4 Comparison of  $U/U_{\max}$  measured with TRDPDV and LDV at  $X/D = 1.6$  and  $Z/H = 0$

velocity gradients and turbulent fluctuations were large, which was just behind the pin fin at  $X/D = 1.6$  and  $Z/H = 0$ . Figures 4 and 5 show  $U/U_{\max}$  and  $u'/U_{\max}$ , respectively, plotted against  $Y/D$ . The results show reasonable agreement across the shear layer and in the pin-fin wake, where there exists highly turbulent flow. It was observed that for  $X/D = 1.6$  the location of the shear layers were similar for  $Re_D = 3.0 \times 10^3$  and  $20 \times 10^3$  as evidenced by the overlap in mean velocity and the peak in fluctuating velocity at  $Y/D = -0.5$ .

### The Horseshoe Vortex Flowfield

As with typical wing-body junction flows, a horseshoe vortex developed upstream of pin fins due to the variation in total pressure in the wall-normal direction from the incoming boundary layer. Figure 6 shows a schematic of the junction between the pin fin and endwall [19]. The horseshoe vortex (HV), secondary vortex (SV), tertiary vortex (TV), and corner vortex (CV) are labeled in the figure.

TRDPDV measurements were made in the stagnation plane  $\theta = 0$  deg to determine the behavior of the HV system. Figure 7 shows contours of mean streamwise velocity normalized by the bulk channel velocity. As Reynolds number increased, the boundary layer profile flattened and the HV moved closer to the cylinder and decreased in size. The streamtraces in Fig. 7 show a complete

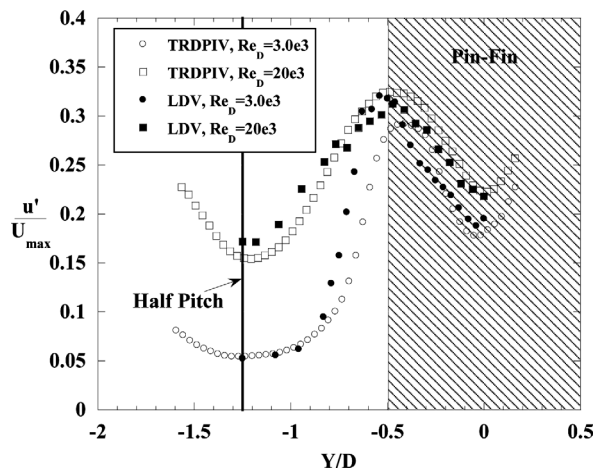


Fig. 5 Comparison of  $u'/U_{\max}$  measured with TRDPDV and LDV at  $X/D = 1.6$  and  $Z/H = 0$

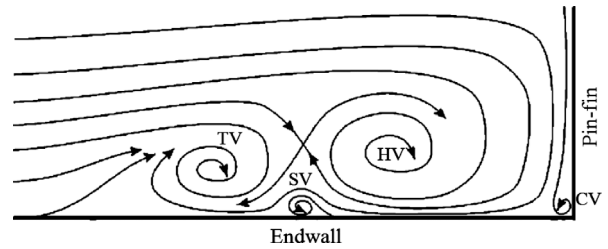


Fig. 6 Features of the horseshoe vortex system at the cylindrical leading edge [19]

roll up at lower Reynolds number due to a more stable HV in comparison to those at higher Reynolds numbers.

The mean swirling strength  $\lambda_{ci}$  was determined by calculating the eigenvalues of the local two-dimensional velocity gradient tensor. If the eigenvalues are complex conjugates,  $\lambda_{ci}$  is equal to the coefficient on the imaginary portion. Isocontours of approximately 95% of the maximum  $\lambda_{ci}$  provide a good threshold for determining the location of coherent structures [31]. Contours showing the local maxima of  $\lambda_{ci}$  are shown in Fig. 7 (dashed lines). The location of the HV, defined by the  $\lambda_{ci}$  maxima, was determined to be  $X/D = -0.80, -0.64,$  and  $-0.62$  for  $Re_D = 3.0 \times 10^3, 10 \times 10^3,$  and  $20 \times 10^3$ , respectively. While the location of the HV is a function of  $\delta/D, Re_D,$  and  $Tu$ , the measured HV locations agreed reasonably well with other wing-body junction flows [8,16,20,21].

For the Reynolds numbers considered in the present work, the HV system oscillated upstream of the obstruction in a quasi-periodic fashion. To quantify the unsteadiness of the HV system, mean normalized turbulent kinetic energy was calculated and is shown in Fig. 8. Note that turbulent kinetic energy was calculated using only the in-plane turbulence components  $u'$  and  $w'$ . The peak turbulent kinetic energy increased with Reynolds number indicating a more unstable HV system at higher Reynolds numbers. The location of maximum turbulent kinetic energy moved closer to the cylinder, which is consistent with the locations of maximum swirl strength in Fig. 7. And regions of high turbulent kinetic energy extended farther upstream at low Reynolds numbers, which may have implications on endwall heat transfer.

Instantaneous realizations of the flowfield at  $\theta = 0$  deg showed similar behavior to previous wing-body junction flow studies. Figures 9 and 10 show instantaneous streamtraces and normalized,

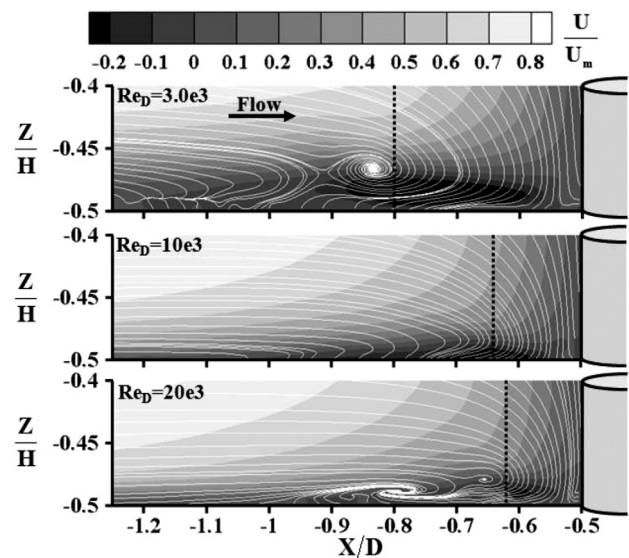


Fig. 7 Mean streamwise velocity contours, streamtraces, and location of peak swirl strength (dashed lines) taken in the stagnation plane

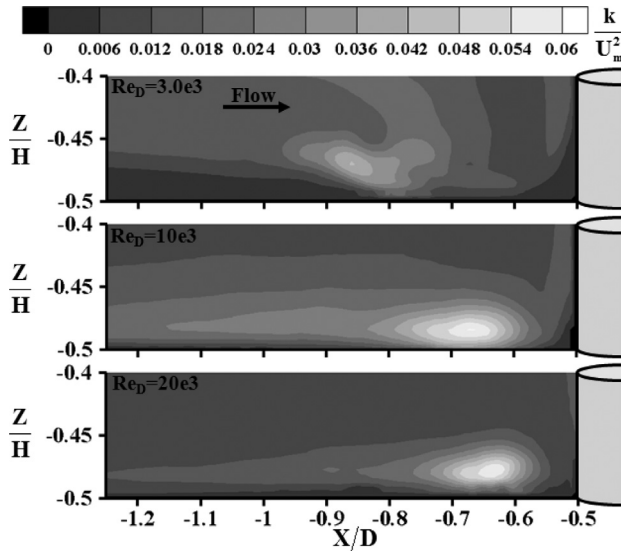


Fig. 8 Normalized turbulent kinetic energy contours taken in the stagnation plane

in-plane velocity magnitude for flow at  $Re_D = 3.0 \times 10^3$  and  $20 \times 10^3$ , respectively. Instantaneous data is shown 0.030 s apart for the low Reynolds number and 0.002 s apart for the high Reynolds numbers, the integrated pressure coefficient  $C_{D,p}$  increased from 0.89 for a single, infinitely long cylinder to 2.22 at the pin-fin midline. At high Reynolds numbers  $C_{D,p}$  increased from 1.20 for a single, infinitely long cylinder to 2.39 at the pin-fin midline.

Previous researchers have decoupled the effects of blockage using velocity through the minimum flow area  $U_{max}$  in the definition of  $C_p$  and  $C_{D,p}$  [24]. In the present work,  $C_{D,p}$  was calculated to be 0.80 at  $Re_D = 3.0 \times 10^3$  and 0.86 at  $Re_D = 20 \times 10^3$  when using  $U_{max}$  as the reference velocity. While the use of  $U_{max}$  has shown to produce a constant drag coefficient for a given Reynolds number at various blockage ratios [24], the resulting  $C_{D,p}$  was slightly lower than that of single, infinitely long cylinders.

### The Near-Wake Flowfield

The pressure distribution at the pin midline for the single row of pin fins was compared with a single, infinitely long cylinder [22] and the first row of a seven row pin-fin array [23]. Figures 11 and 12 show  $C_p$  measured at the pin midline for low and high Reynolds numbers, respectively. To compare the present results to a single, infinitely long cylinder,  $C_p$  was calculated using bulk

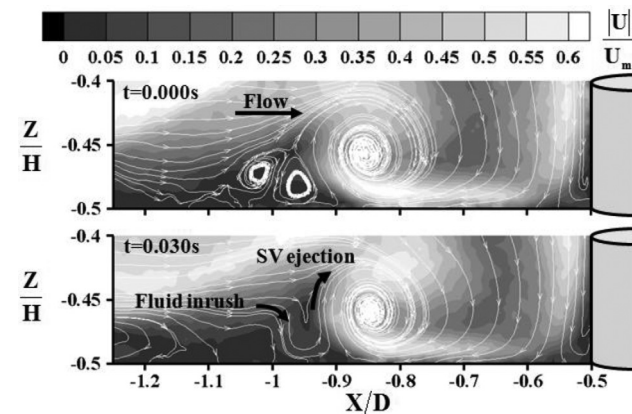


Fig. 9 Instantaneous contours of normalized streamwise velocity and instantaneous streamtraces showing the HV system at  $Re_D = 3.0 \times 10^3$

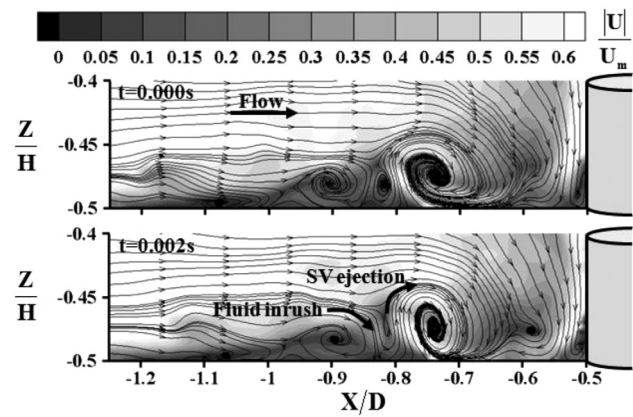


Fig. 10 Instantaneous contours of normalized streamwise velocity and instantaneous streamtraces showing the HV system at  $Re_D = 20 \times 10^3$

channel velocity  $U_m$  in the definition of  $C_p$ . The effect of blockage was evident at angles as low as 40 deg where flow around the pin fins was accelerated resulting in reduced pressure coefficients. The increased suction at the backside of the pin fin resulted in a higher drag coefficient than the single cylinder. At low Reynolds numbers, the integrated pressure coefficient  $C_{D,p}$  increased from 0.89 for a single, infinitely long cylinder to 2.22 at the pin-fin midline. At high Reynolds numbers  $C_{D,p}$  increased from 1.20 for a single, infinitely long cylinder to 2.39 at the pin-fin midline.

In comparison with the multirow array investigated by Ames and Dvorak [23], the present results showed good agreement at both low and high Reynolds numbers. This result indicated that the presence of downstream rows does not significantly impact the mean pressure distribution at the pin midline of the first row for this particular pin-fin spacing.

The near-wake flow structure was investigated with two-component LDV and TRDPIV. TRDPIV was used to compliment the LDV data in providing instantaneous vector fields. Figure 13

Midline  $C_p$  versus  $\theta$  at  $Re_D = 3.0 \times 10^3$  [22,23]

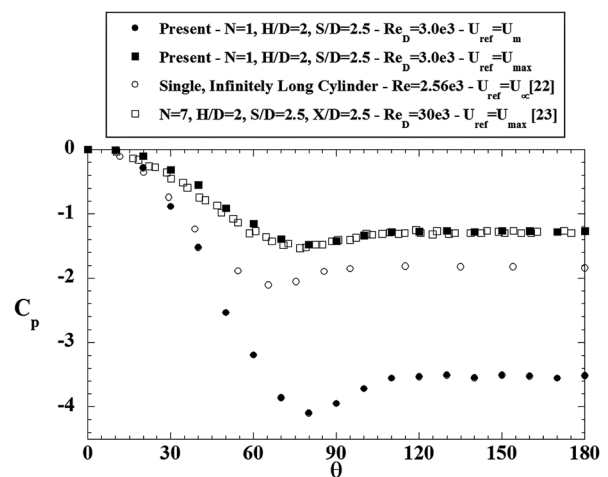


Fig. 11 Midline  $C_p$  versus  $\theta$  at  $Re_D = 3.0 \times 10^3$  [22,23]

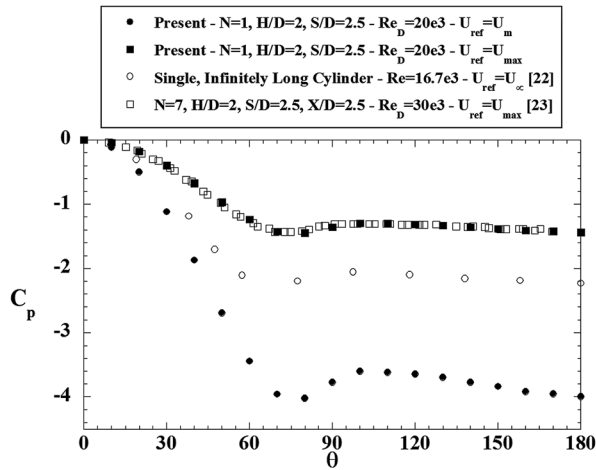


Fig. 12 Midline  $C_p$  versus  $\theta$  at  $Re_D = 20 \times 10^3$  [22,23]

shows contours of normalized streamwise velocity in the near wake at  $Re_D = 3.0 \times 10^3$ ,  $10 \times 10^3$ , and  $20 \times 10^3$ . The TRDPIV data is shown for comparison in Fig. 13 indicating excellent agreement with the LDV data.

The wake length,  $L_c$  is defined as the point along the wake centerline where the mean streamwise velocity is zero [22]. The wake length is shown graphically in Fig. 13 where the streamtraces form a saddle point (solid white arrows). It was observed that  $L_c$  decreased between  $Re_D = 3.0 \times 10^3$  and that of  $Re_D = 10 \times 10^3$  and  $20 \times 10^3$ .

Previous studies have reported that wake length and other characteristic length scales generally follow the vortex formation length  $L_f$ , where the Kármán vortices (KV) are fully formed [22]. Although  $L_f$  is defined as the point of minimum  $C_p$  along the wake centerline, the point of maximum streamwise rms velocity is a good approximation [25] and was used in the present work. Figure 14 shows  $L_f/D$  reported for different Reynolds numbers. Single, infinitely long cylinder data is shown for comparison as solid sym-

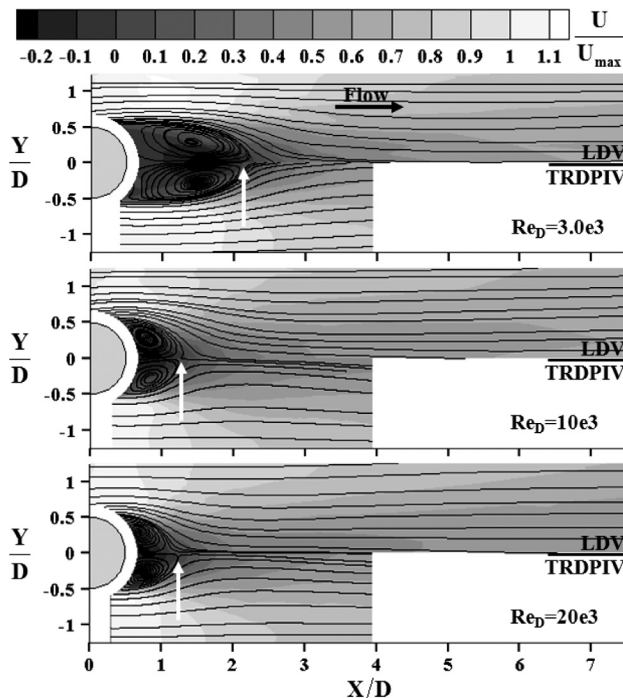


Fig. 13 Mean streamwise velocity and streamtraces behind the pin fin at the channel centerline

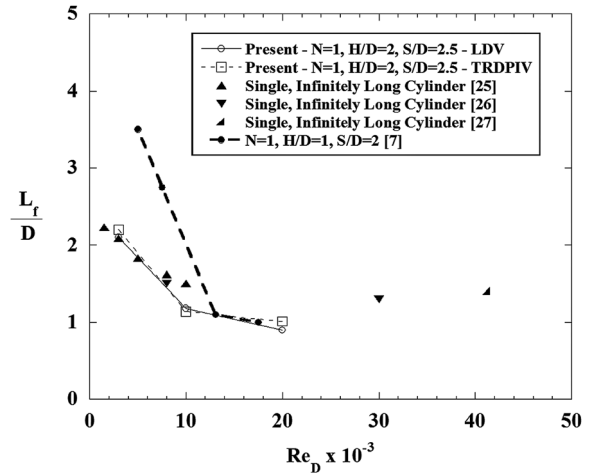


Fig. 14 Formation length versus  $Re$  for the present study (single-row,  $H/D = 2$ ,  $S/D = 2.5$ ) and for single, infinitely long cylinders [7,25–27]

bol. The data indicated that the KV developed closer to the cylinder with increasing Reynolds number. The shortened formation length was due to the increased suction pressure along the downstream side of the pin fin. Also, the blockage-induced local acceleration led to strengthened KVs that were able to develop closer to the pins. For the low Reynolds number, however, the KVs developed farther downstream in a more equilibrated location. Transitional mixing occurred along the elongated shear layer and counteracted the effects of blockage by slowing the high momentum fluid that supplied energy to the KVs. Therefore,  $L_f$  was similar to that of single cylinders at  $Re_D = 3.0 \times 10^3$ .

The instantaneous flowfield was captured with the TRDPIV system allowing for a detailed view of the near-wake dynamics in space and time. Figure 15 shows instantaneous streamtraces and normalized, in-plane velocity magnitude contours at  $Re_D = 3.0 \times 10^3$  in 0.010 s increments corresponding to 0.10 shedding cycles. Similarly, Fig. 16 shows instantaneous data at  $Re_D = 20 \times 10^3$  in 0.002 s increments corresponding to 0.11 shedding cycles. The size of the KV followed the trend of wake length and formation length and decreased between  $Re_D = 3.0 \times 10^3$  and that of  $Re_D = 10 \times 10^3$  and  $20 \times 10^3$ . The KV was about one cylinder diameter in size at low Reynolds numbers and about 0.5 cylinder diameters in size at high Reynolds numbers.

Several marked differences in the vortex shedding process were observed in the TRDPIV measurements when comparing low and high Reynolds number cases. At low Reynolds number, the instantaneous TRDPIV data showed the KV forming downstream, detached from the pin fin. At high Reynolds numbers, however, the KV was observed to develop adjacent to the pin fin. This observation was verified in Figs. 11 and 12 where a local minima was present at  $\theta = 180$  deg for  $Re_D = 20 \times 10^3$  but not for  $Re_D = 3.0 \times 10^3$ . Furthermore, the KV was observed to remain on the same side of the wake in which it was formed when  $Re_D = 3.0 \times 10^3$ . At  $Re_D = 20 \times 10^3$ , however, the KV crossed the wake centerline after being shed from the pin fin. It can be expected that the formation of the KV adjacent to the pin fin and the subsequent cross-wake trajectory of the KV at high Reynolds numbers will impact the pin fin and endwall heat transfer.

At both low and high Reynolds numbers, shear layer vortices were observed to distort the shape of the KV and increase its unsteadiness. The shear layer vortices may play a role in pin surface and endwall heat transfer, although the KV can be expected to govern wake heat transfer. Shear layer vortices may indirectly affect heat transfer, either favorably or adversely. Mechanisms for affecting heat transfer include causing a more rapid breakdown of the KV and increasing random turbulent motions in the wake.

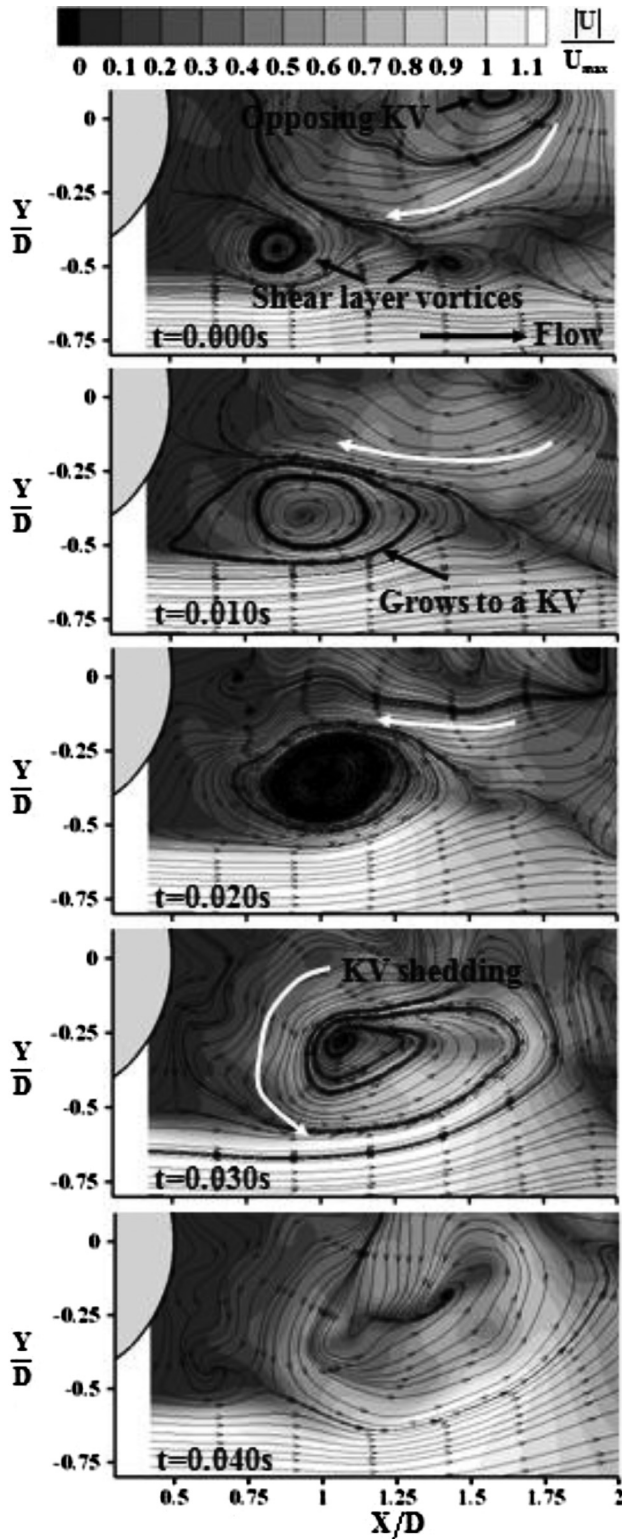


Fig. 15 Instantaneous streamtraces at  $Re_D = 3.0 \times 10^3$  where the images are taken 0.10 shedding cycles apart

Spectral analyses were performed in the wake at the point:  $X/D = 1.6$ ,  $Y/D = 0$ ,  $Z/H = 0$ . The vortex shedding frequency was calculated by performing a fast Fourier transform (FFT) on the transverse velocity signal. LDV data was down sampled using nearest-neighbor interpolation to obtain a regularly spaced time series. The frequency response of the down-sampled LDV data was at least 25 times that of the measured shedding frequency and data was collected over at least 300 shedding cycles. The TRDPDV

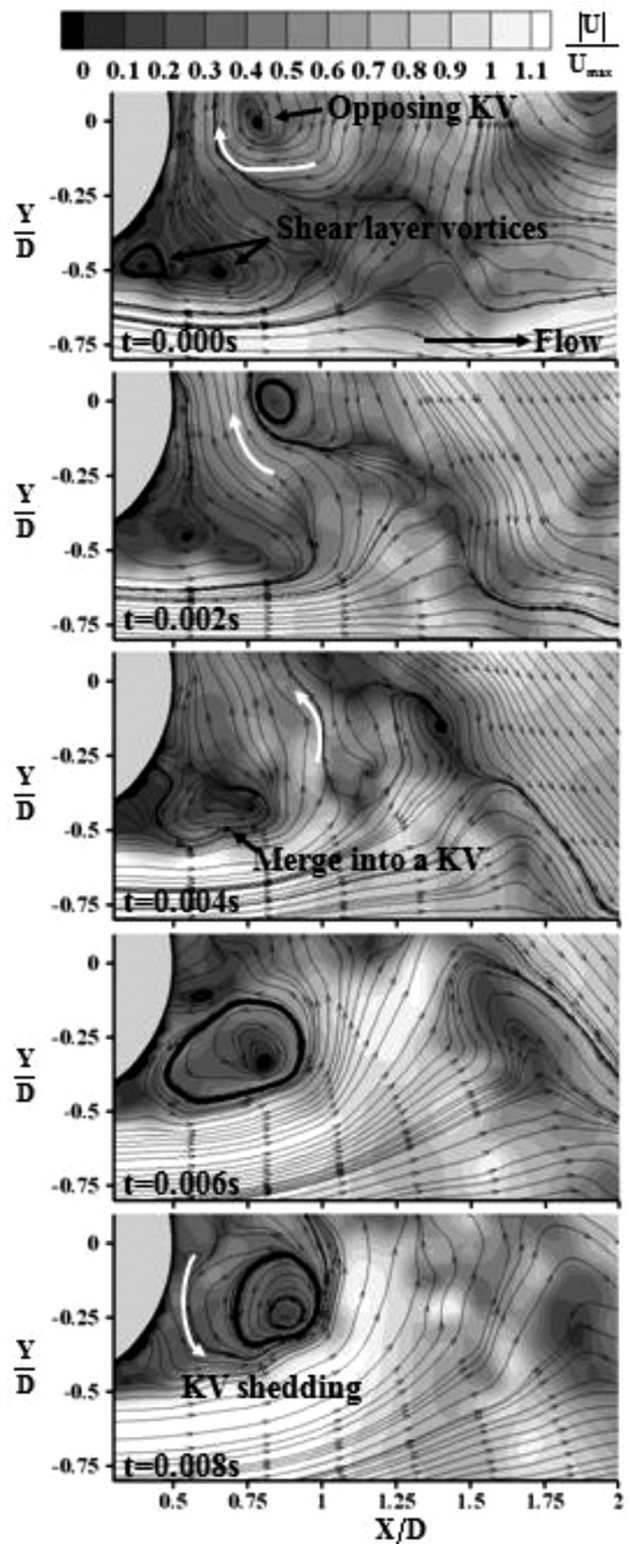


Fig. 16 Instantaneous streamtraces at  $Re_D = 20 \times 10^3$  where the images are taken 0.11 shedding cycles apart

data was sampled at 17 times that of the measured shedding frequency for a minimum of 50 shedding cycles. Both TRDPDV and LDV data were weighted using a Hanning window, although using a rectangular window showed no significant leakage at the measured peaks.

Table 3 shows the Strouhal frequency measured for the single row configuration. Also shown in Table 3 are results from a

**Table 3 Strouhal numbers of the pin fins**

$Re_D$	Present: LDV	Present: TRDPIV	Single, infinitely long cylinder [22]	Row 1 of multirow array [28]
$3.0 \times 10^3$	0.21	0.21	0.21	0.23
$10 \times 10^3$	0.17	0.17	0.20	0.23
$20 \times 10^3$	0.17	0.18	0.19	—
$30 \times 10^3$	—	—	—	0.21

single, infinitely long cylinder [22] and a multirow configuration [28]. It should be noted that the pin-fin data makes use of  $U_{max}$  as the reference velocity in the definition of  $St$ . It was found that the present, single row Strouhal frequency matched that of single, infinite cylinders at  $Re_D = 3.0 \times 10^3$ . At higher Reynolds numbers, however, the present results show a decreasing Strouhal frequency. The use of  $U_{max}$  as the reference velocity; therefore, does not effectively decouple the effect of blockage ratio on Strouhal frequency. The present, single row Strouhal frequencies were lower than those reported by Ames et al. for a multiple row pin-fin array [28]. In multirow arrays, the presence of a downstream row imposed a constraint on the width of the near wake which increased the shedding frequency.

**Correlation With Heat Transfer**

Lyall et al. [7] reported significant heat transfer contributions from the KV for single rows of pin fins having various span-to-diameter ratios and a height-to-diameter ratio of unity. Comparisons made between the present work and that of Lyall et al. [7] were validated by the findings of Brigham and VanFossen [9] which showed little difference in array-averaged heat transfer for  $1 \leq H/D \leq 2$ . Also, Lyall et al. [7] investigated  $S/D = 2$ , which is similar to the present spacing of  $S/D = 2.5$ . The location of maximum heat transfer measured by Lyall et al. [7] was included in the plot of KV formation length versus Reynolds number, Fig. 14. The location of peak heat transfer approximately followed the trend of KV formation length for the present configuration indicating that the KV plays an important role on heat transfer.

For these single row configurations, two regimes were identified that describe the formation of the KV. At low Reynolds numbers, less than  $Re_D = 10 \times 10^3$ , a regime was identified where the KV was detached from the pin fin and required at least one pin diameter downstream to become fully formed. At high Reynolds numbers, greater than  $Re_D = 10 \times 10^3$ , the KV formed adjacent to the pin fin within one pin diameter of the pin-fin center. These regimes were originally identified for single, infinitely long cylinders where the higher Reynolds number regime showed the shear layer transitioning to turbulence closer to the pin fin as well as the KV forming closer to the pin fin [22].

Because the location of maximum heat transfer roughly followed the development of the KV, comparisons were made between endwall heat transfer [7] and turbulent fluctuations. Figure 17 shows augmentation of  $u'$  and Fig. 18 shows augmentation of  $v'$  where each turbulent component is normalized by that measured at the core of an unobstructed duct. Endwall heat transfer augmentation contours are shown for comparison on the bottom halves of each figure. As expected from the approximate agreement between KV formation length and location of peak heat transfer in Fig. 14, regions of high heat transfer augmentation were found to agree with regions of high turbulence augmentation in Figs. 17 and 18. The regions of peak endwall heat transfer showed detachment from the pin fins at low Reynolds number and approached the trailing edge of the pin fin at Reynolds numbers greater than  $10 \times 10^3$ . It was found that the large scale unsteady motions of the KV contributed to the regions of high turbulence augmentation.

The trajectory of the KV caused regions of high  $u'/u'_o$  in the shear layer and high  $v'/v'_o$  in the wake. The transverse fluctuations

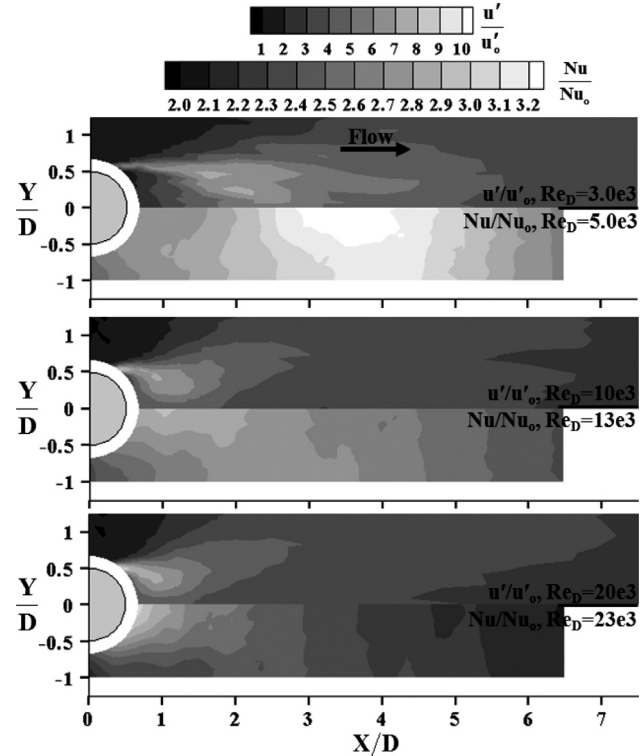


**Fig. 17 Streamwise fluctuation augmentation and endwall heat transfer augmentation [7]**

showed contour patterns that resembled heat transfer contours more closely than streamwise fluctuations. It was likely that the KV entrained core fluid at the shear layer, and then as the KV crossed the wake, the KV broke down into stochastic turbulence and allowed turbulent mixing to occur.

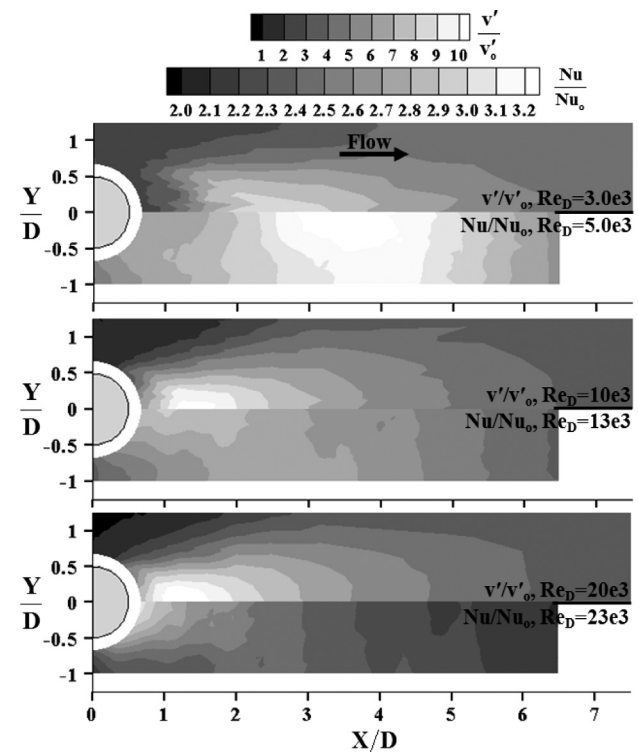


**Fig. 18 Transverse fluctuation augmentation and endwall heat transfer augmentation [7]**

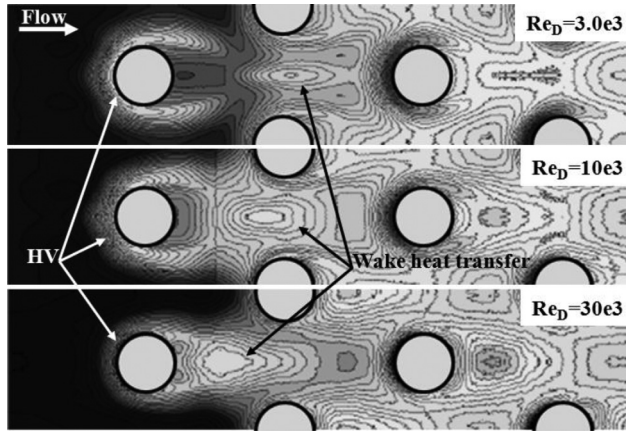


**Fig. 19 Mean endwall heat transfer contours in a multirow pin-fin array ( $H/D=2$ ,  $S/D=X/D=2.5$ ) [6]**

Endwall heat transfer contours taken by Ames et al. [6], shown in Fig. 19, provide evidence that the horseshoe vortex contributes significantly to endwall heat transfer in typical pin-fin arrays. In the first row, the HV enhanced heat transfer adjacent to the pin fin between  $\theta=0$  deg and  $90$  deg with a region of enhanced heat transfer extending tangent to  $\theta=90$  deg. In the stagnation plane, the HV heat transfer footprint moved closer to the pin fin as Reynolds number increases in agreement with the present TRDPIV measurements.

It was shown that the KV contributes largely to single row heat transfer. The Kármán vortices also contribute largely to heat transfer for multiple row pin-fin arrays. Ames et al. [6] observed enhanced heat transfer in the pin-fin wakes as indicated in Fig. 19. And Ames et al. [6] were able to detect a characteristic shedding frequency, reported in Table 2. This suggests that the downstream rows did not completely inhibit vortex shedding for the spacing of  $S/D=2.5$ ,  $X/D=2.5$ . Despite the presence of the downstream rows, the peak heat transfer approached the pin fin as Reynolds number increased, similar to the single row configuration. This suggests that the KV plays a large role in heat transfer for multiple row arrays as well as the present, single row configuration. Future investigations will characterize the development of the KV in multiple row arrays and what affect the KV has on endwall heat transfer.

## Conclusions

A single row of pin fins having  $H/D=2$ ,  $S/D=2.5$  was investigated using two-component laser Doppler velocimetry and time-resolved digital particle image velocimetry. Both the horseshoe vortex system and the near-wake flow were investigated and comparisons were made with similar fundamental studies.

The horseshoe vortex system was found to behave similarly to typical wing-body junction flows. At the lowest Reynolds number, the horseshoe vortex was found to be more stable than at high Reynolds numbers and was found to affect a larger area upstream of the obstruction. In a multiple row array of similar geometry, heat transfer enhancement followed this trend of moving closer to the pin fin with increasing Reynolds number.

The near wake flow showed characteristics of cylinders in crossflow under the influence of blockage. The streamwise pressure gradients resulted in a more negative pressure at the downstream side of the pin fins in comparison to a single, infinite cylinder. This increased suction on the backside of the pin fin in combination with stronger Kármán vortices resulted in a shortened distance required for the Kármán vortices to form at high Reynolds numbers.

It was found that the location of maximum endwall heat transfer in the pin-fin wake approximately followed the Kármán vortex

formation length. Transverse velocity fluctuations were found to agree with the locations of high endwall heat transfer in the wake indicating that the Kármán vortices were the driving flow mechanism for augmenting wake heat transfer. The Kármán vortices efficiently entrained core fluid and transported that fluid into the wake where turbulent mixing allowed effective heat transfer to occur.

## Acknowledgment

The authors would like to acknowledge the Science, Math, and Research for Transformation (SMART) fellowship program and the Department of Defense (DoD) for sponsoring this work.

## Nomenclature

- $C_{D,p}$  = form drag contribution to drag coefficient  
 $C_p$  = pressure coefficient,  $C_p = \frac{P(\theta) - P(\theta=0^\circ)}{0.5\rho U_{ref}^2}$   
 $D$  = pin-fin diameter  
 $D_h$  = hydraulic diameter  
 $f$  = friction factor  
 $f_k$  = vortex shedding frequency  
 $f_o$  = baseline friction factor,  $f_o = [1.5635 \cdot \ln(\text{Re}/7)]^{-2}$  [29]  
 $h$  = heat transfer coefficient  
 $H$  = channel height and length of pin fins  
 $k$  = turbulent kinetic energy,  $k = 0.5(u'^2 + w'^2)$ ; thermal conductivity  
 $Nu$  = Nusselt number,  $Nu = hD_h/k^{-1}$   
 $Nu_o$  = baseline Nusselt number,  $Nu_o = 0.023\text{Re}^{0.8}\text{Pr}^{0.4}$  [30]  
 $P$  = static pressure  
 $\text{Pr}$  = Prandtl number  
 $\text{Re}$  = duct Reynolds number,  $\text{Re} = U_m D_h \nu^{-1}$   
 $\text{Re}_D$  = pin-fin Reynolds number,  $\text{Re}_D = U_{max} D \nu^{-1}$   
 $S$  = transverse spacing of pin fins  
 $\text{St}$  = Strouhal number,  $\text{St} = f_k D (U_{max})^{-1}$   
 $t$  = time  
 $U_{95}$  = total uncertainty for 95% confidence interval  
 $U_{bias}$  = bias uncertainty  
 $U, V, W$  = mean velocity components  
 $u', v', w'$  = rms velocity components  
 $X$  = streamwise direction; streamwise spacing of pins  
 $Y$  = transverse direction  
 $Z$  = wall-normal direction
- Greek**  
 $\lambda_{ci}$  = swirling strength [31]  
 $\nu$  = kinematic viscosity  
 $\theta$  = circumferential location on cylinder

## Subscripts

- $\infty$  = freestream velocity  
 $m$  = bulk velocity  
 $\text{max}$  = mean velocity through minimum flow area  
 $\text{ref}$  = reference velocity  
 $o$  = unobstructed duct value

## References

- [1] Incropera, F. P., and Dewitt, D. P., 2002, *Fundamentals of Heat and Mass Transfer*, 5th ed., John Wiley, New York.
- [2] Metzger, D. E., and Haley, S. W., 1982, "Heat Transfer Experiments and Flow Visualization for Arrays of Short Pin Fins," ASME Paper No. 82-GT-138.
- [3] Simoneau, R. J., and VanFossen, G. J., Jr., 1984, "Effect of Location in an Array on Heat Transfer to a Short Cylinder in Crossflow," *ASME J. Heat Transfer*, **106**, pp. 42–48.
- [4] Ames, F. E., Dvorak, L. A., and Morrow, M. J., 2005, "Turbulent Augmentation of Internal Convection Over Pins in Staggered-Pin Fin Arrays," *ASME J. Turbomach.*, **127**(1), pp. 183–190.
- [5] Metzger, D. E., Berry, R. A., and Bronson, J. P., 1982, "Developing Heat Transfer in Rectangular Ducts With Staggered Arrays of Short Pin Fins," *ASME J. Heat Transfer*, **104**(4), pp. 700–706.
- [6] Ames, F. E., Nordquist, C. A., and Klennert, L. A., 2007, "Endwall Heat Transfer Measurements in a Staggered Pin Fin Array With an Adiabatic Pin," ASME Paper No. GT2007-27432.
- [7] Lyall, M. E., Thrift, A. A., Kohli, A., and Thole, K. A., 2007, "Heat Transfer From Low Aspect Ratio Pin Fins," ASME Paper No. GT2007-27431.

- [8] Ozturk, N. A., Akkoca, A., and Sahin, B., 2008, "PIV Measurements of Flow Past a Confined Cylinder," *Exp. Fluids*, **44**, pp. 1001–1014.
- [9] Brigham, B. A., and VanFossen, G. J., 1984, "Length to Diameter Ratio and Row Number Effects in Short Pin Fin Heat Transfer," *ASME J. Eng. Gas Turbines Power*, **106**(1), pp. 241–244.
- [10] Chyu, M. K., Siw, S. C., and Moon, H. K., 2009, "Effects of Height-to-Diameter Ratio of Pin Element on Heat Transfer From Staggered Pin-Fin Arrays," ASME Paper No. GT2009-59814.
- [11] Metzger, D. E., Fan, C. S., and Haley, S. W., 1984, "Effects of Pin Shape and Array Orientation on Heat Transfer and Pressure Loss in Pin Fin Arrays," *ASME J. Eng. Gas Turbines Power*, **106**(1), pp. 252–257.
- [12] Uzol, O., and Camci, C., 2005, "Heat Transfer, Pressure Loss and Flow Field Measurements Downstream of Staggered Two-Row Circular and Elliptical Pin Fin Arrays," *ASME J. Heat Transfer*, **127**(5), pp. 458–471.
- [13] Raffel, M., Willert, C., Wereley, S., and Kompenhans, J., 1998, *Particle Image Velocimetry: A Practicle Guide*, Springer, New York.
- [14] Nogueira, J., Lecuona, A., and Rodriguez, P. A., 1997, "Data Validation, False Vectors Correction and Derived Magnitudes Calculation on PIV Data," *Meas. Sci. Technol.*, **8**, pp. 1493–1501.
- [15] Moffat, R. J., 1988, "Describing the Uncertainties in Experimental Results," *Exp. Thermal Fluid Sci.*, **1**(1), pp. 3–17.
- [16] Radomsky, R. W., and Thole, K. A., 2000, "High Free-Steam Turbulence Effects on Endwall Heat Transfer for a Gas Turbine Stator Vane," *ASME J. Turbomach.*, **122**, pp. 699–708.
- [17] Scarano, F., and Riethmuller, M. L., 2000, "Advances in Iterative Multigrid PIV Image Processing," *Exp. Fluids*, **29**, pp. S051–S060.
- [18] Harder, K. J., and Tiederman, W. G., 1991, "Drag Reduction and Turbulent Structure in Two-Dimensional Channel Flows," *Phil. Trans. R. Soc. Ser. A*, **336**, pp. 19–34.
- [19] Praisner, T. J., and Smith, C. R., 2006, "The Dynamics of the Horseshoe Vortex and Associated Endwall Heat Transfer—Part I: Temporal Behavior," *ASME J. Turbomach.*, **128**(4), pp. 747–754.
- [20] Praisner, T. J., and Smith, C. R., 2006, "The Dynamics of the Horseshoe Vortex and Associated Endwall Heat Transfer—Part II: Time-Mean Results," *ASME J. Turbomach.*, **128**(4), pp. 755–762.
- [21] Devenport, W. J., and Smith, R. L., 1990, "Time-Dependent and Time-Averaged Turbulence Structure Near the Nose of a Wing-Body Junction," *J. Fluid Mech.*, **210**, pp. 23–55.
- [22] Zdravkovich, M. M., 1997, *Flow Around Circular Cylinders - Volume 1: Introduction*, Oxford University Press, New York.
- [23] Ames, F. E., and Dvorak, L. A., 2006, "The Influence of Reynolds Number and Row Position on Surface Pressure Distributions in Staggered Pin Fin Arrays," ASME Paper No. GT2006-90170.
- [24] Zdravkovich, M. M., 2003, *Flow Around Circular Cylinders - Volume 2: Applications*, Oxford University Press, New York.
- [25] Norberg, C., 2003, "Fluctuating Lift on a Circular Cylinder: Review and New Measurements," *J. Fluids Struct.*, **17**(1), pp. 57–96.
- [26] Norberg, C., and Sunden, B., 1987, "Turbulence and Reynolds Number Effects on the Flow and Fluid Forces on a Single Cylinder in Cross Flow," *J. Fluids Struct.*, **1**(3), pp. 337–357.
- [27] Ünal, U., and Atlar, M., 2010, "An Experimental Investigation into the Effect of Vortex Generators on the Near-Wake Flow of a Circular Cylinder," *Exp. Fluids*, **48**(6), pp. 1059–1079.
- [28] Ames, F. E., and Dvorak, L. A., 2005, "Turbulent Transport in Pin Fin Arrays—Experimental Data and Predictions," ASME Paper No. GT2005-68180.
- [29] Colebrook, C. F., 1939, "Turbulent Flow in Pipes, With Particular Reference to the Transition Region Between the Smooth and Rough Pipe Laws," *J. Inst. Civil Eng.*, **4**, pp. 133–156.
- [30] McAdams, W. H., 1942, *Heat Transmission*, McGraw-Hill, New York.
- [31] Adrian, R. J., Christensen, K. T., and Liu, Z. C., 2000, "Analysis and Interpretation of Instantaneous Turbulent Velocity Fields," *Exp. Fluids*, **29**(3), pp. 275–290.